

Super-Reversible CuF_2 Cathodes Enabled by Cu^{2+} -Coordinated Alginate

Jiale Xia, Zeyi Wang, Nuwanthi D. Rodrig, Bo Nan, Jiaxun Zhang, Weiran Zhang, Brett L. Lucht, Chongyin Yang,* and Chunsheng Wang*

Copper fluoride (CuF_2) has the highest energy density among all metal fluoride cathodes owing to its high theoretical potential (3.55 V) and high capacity (528 mAh g^{-1}). However, CuF_2 can only survive for less than five cycles, mainly due to serious Cu-ion dissolution during charge/discharge cycles. Herein, copper dissolution is successfully suppressed by forming Cu^{2+} -coordinated sodium alginate (Cu-SA) on the surface of CuF_2 particles during the electrode fabrication process, by using water as a slurry solvent and sodium alginate (SA) as a binder. The trace dissolved Cu^{2+} in water from CuF_2 can in situ cross-link with SA binder forming a conformal Cu-SA layer on CuF_2 surface. After water evaporation during the electrode dry process, the Cu-SA layer is Li-ion conductor but Cu^{2+} insulator, which can effectively suppress the dissolution of Cu-ions in the organic 4 M LiClO_4 /ethylene carbonate/propylene carbonate electrolyte, enhancing the reversibility of CuF_2 . CuF_2 electrode with SA binder delivers a reversible capacity of 420.4 mAh g^{-1} after 50 cycles at 0.05 C, reaching an energy density of 1009.1 Wh kg^{-1} . Cu^{2+} cross-link polymer coating on CuF_2 opens the door for stabilizing the high-energy and low-cost CuF_2 cathode for next-generation Li-ion batteries.

decades.^[1] The energy density of current commercial LIBs is limited by the layer-structured cathodes (such as LiCoO_2 and $\text{LiNi}_x\text{Mn}_y\text{Co}_{1-x-y}\text{O}_2$), which can only provide a specific capacity of less than 220 mAh g^{-1} due to the limited Li^+ host sites in the materials' lattice.^[2] In addition, the rapid expansion of LIBs market leads to a surge in Co and Ni prices (up to 90 USD kg^{-1} for Co metal, 2022). Therefore, exploring Co- and Ni-free cathode materials with high energy densities and low costs are in urgent need.

Conversion-type materials, which usually consist of less expensive and environment friendly elements such as Fe, Cu, O, and S, have much higher capacity than intercalation-type electrode materials.^[3] Among various conversion compounds, transition metal fluorides (MF_x) provides both high redox potentials of >2.0 V (owing to the high ionicity of the metal–fluoride bond) and a large capacity

by allowing multiple electrons transfer per unit formula, thus enabling significant high theoretical energy densities.^[4] One major challenge for conversion cathode is the cycle stability. The optimized Fe-based fluorides such as FeF_2 , FeF_3 , FeOF , and $\text{Fe}_{0.9}\text{Co}_{0.1}\text{OF}$ can stably charge/discharge for few hundred cycles.^[5] However, the energy density of Fe-based cathode is still not high enough. Copper fluoride (CuF_2) offers an much higher specific energy density (1874 Wh kg^{-1}) than Fe-based fluorides due to its high theoretical potential of 3.55 V versus Li/Li⁺ and theoretical capacity of 528 mAh g^{-1} .^[6]

The reversible conversion reactions of CuF_2 follow the following process:



However, CuF_2 can only charge/discharge for few cycles. The CuF_2 conversion reaction suffers from four critical challenges: 1) The intrinsically poor electronic conductivity induced by the highly ionic character of Cu–F bond reduces reaction reversibility and kinetics, resulting in a low Coulombic efficiency and extremely poor rate capabilities. 2) Large voltage hysteresis (≈ 1 V) due to the large activation energy barrier for breaking chemical bonds like Cu–F and Li–F during the lithiation and delithiation process reduces energy efficiency and accessible energy.^[7] 3) The aggregation and continuous coarsening of Cu

1. Introduction

Lithium-ion batteries (LIBs) have been used as a power source for portable devices and electric vehicles over the past

J. Xia, Z. Wang, B. Nan, J. Zhang, W. Zhang, C. Wang
Department of Chemical and Biomolecular Engineering
University of Maryland
College Park, MD 20742, USA
E-mail: cswang@umd.edu

J. Xia
Frontier Institute of Science and Technology
Xi'an Jiaotong University
Xi'an, Shaanxi 710054, China

N. D. Rodrig, B. L. Lucht
Department of Chemistry
University of Rhode Island
South Kingstown, RI 02881, USA

C. Yang
Department of Physics and Atmospheric Science
Dalhousie University
Halifax, Nova Scotia B3H 4R2, Canada
E-mail: c.yang@dal.ca

 The ORCID identification number(s) for the author(s) of this article can be found under <https://doi.org/10.1002/adma.202205229>.

DOI: 10.1002/adma.202205229

nanoparticles due to the high mobility of copper ions, induce phase separation between LiF and Cu nanoparticles, discontinuing the conductive network and reducing reconversion reaction kinetics.^[8] 4) Serious dissolution of active materials during charge process results in irreversible capacity loss, which has been regarded as the direct reason for the irreversibility of CuF₂ cathode.^[7b,9]

Extensive research has been conducted to solve these challenges. However, only limited advance has been achieved. To enhance the reaction kinetics, nanosized CuF₂ particles were imbedded in a mixed conductive matrix, enabling CuF₂ to provide a near-theoretical capacity of CuF₂ for only one discharge.^[10] Dispersing CuF₂ nanoparticles into mesoporous carbon can achieve a capacity of 510 mAh g⁻¹ for first discharge, but quickly faded to 280 mAh g⁻¹ after five cycles due to Cu-ion dissolution.^[11] To suppresses the Cu-ion dissolution, a NiO layer was coated on CuF₂ electrode to serve as an artificial CEI layer to prevent the direct contact between CuF₂ and electrolyte.^[12] However, the NiO-CuF₂/C electrode only provides a capacity of ≈100 mAh g⁻¹ for three cycles. Recently, a ternary metal fluoride of Cu_{0.5}Fe_{0.5}F₂ was reported to enhance the reversible Cu²⁺/0 reaction because the substitution of Fe ions could promote the reconversion of Cu to form a rutile-like Cu-Fe-F phase.^[7a] However, Cu_{0.5}Fe_{0.5}F₂ only achieves five cycles. Subsequent research turns out that the improved cycling stability of Cu_{0.5}Fe_{0.5}F₂ is attributed to a combination of activity of Fe²⁺/Fe₀ and Fe³⁺/Fe²⁺ rather than Cu²⁺/Cu⁰ redox couples.^[9] Up to now, the copper-ion dissolution problem remains unsolved, and the CuF₂ can only be charged/discharged for five cycles. An approach other than (CuM)F₂ alloy should be explored.

It has been reported that sodium alginate (SA) can be cross-linked by multivalent cations (Cu²⁺, Ba²⁺, Ca²⁺, Mn²⁺, Al³⁺) forming a multivalent cation insulating network structure,^[13] which can significantly suppress the dissolution of multivalent cations. A Cu²⁺-cross-linked SA membrane can block multivalent cations but provide nanoscale channels for selective and fast transport of Li⁺, Na⁺, and K⁺ ions in high salt solutions without structure distortion.^[14] In addition, SA is also an excellent binder for enhanced battery performance due to its low cost, low toxicity, and high mechanical properties.^[15] The Ba²⁺- or Al³⁺-cross-linked SA binder has been reported to significantly suppress the capacity and voltage fading of Li-rich and Mn-based oxide cathodes by inhibiting the Mn dissolution.^[16] In addition, the cross-linked SA binder has a high mechanical strength enabling silicon and silicon-carbon anodes to achieve a long cycle life.^[17]

Inspired by Mn dissolution suppression from Ba²⁺-cross-linked SA, herein, we reported that CuF₂ dissolution in organic electrolyte can be suppressed by simply fabricating CuF₂ electrode using SA binder and water solvent. After mixing of CuF₂, water, and SA into the electrode slurry, trace dissolved Cu²⁺ from CuF₂ cross-linked with SA in the slurry forming a conformal coating layer on the surface of CuF₂ particles during electrode fabrication process. The Cu²⁺-cross-linked SA enables the Li⁺ transportation but it blocks Cu²⁺ transport, thus significantly suppressing the copper dissolution of CuF₂ cathode in organic electrolytes during charge/discharge cycles. Due to the moisture sensitive nature of CuF₂, CuF₂ converted into hydrated Cu(OH)F and CuF₂·2H₂O after mixing with water

during electrode coating process. Similar to anhydrous CuF₂, these hydrated CuF₂ (H-CuF₂) also experience a conversion reaction with Li at ≈3.0 V.^[10a,18] The H-CuF₂-SA electrode can deliver a reversible capacity of 420.4 mAh g⁻¹ for 50 cycles at 0.05 C, reaching an extraordinarily high energy density of ≈1009.1 Wh kg⁻¹, which is higher than most of metal fluorides, demonstrating the best performance of Cu-based fluoride cathodes.

2. Results and Discussion

2.1. Formation and Characterization of Cu-SA Layer on CuF₂ Nanoparticles Surface

As a natural polysaccharide extracted from brown algae, SA is a family of copolymer of α-L-guluronic units (G block) and β-D-mannuronic units (M block) which contains plenty of hydroxy and carboxyl groups (Figure 1a). These electric-rich functional groups with polar oxygen atoms in G blocks can cross-link with multivalent cations and form a robust network structure. When the dilute CuF₂ aqueous solution was dropwise added into SA aqueous solution, SA molecules immediately interacted with Cu²⁺ ions and form a blue Cu²⁺-coordinated sodium alginate (Cu-SA) hydrogel with a “egg-box structure” (Figure 1b). The strong cross-linking between the SA and Cu²⁺ ions was characterized using Fourier transform infrared (FTIR). In order to minimize the strong -OH group signal of free water, the Cu-SA hydrogels were dried and grounded to powder before FTIR measurement. As shown in Figure 1c, SA powder exhibits a broad absorption band at ≈3300 cm⁻¹ related to hydrogen-bonded O-H stretching vibrations and a series of sharp peaks at the range of 1000 to 1700 cm⁻¹ corresponded to C-O bonds.^[19] After cross-linking with Cu²⁺ ions, an obvious blue shift of C-O absorption peaks occurred. The peaks located at 1592, 1406, and 1026 cm⁻¹ which are related to asymmetric/symmetric vibrations of COO⁻ and asymmetric vibrations of C-O-C group, shifted to 1608, 1412, and 1032 cm⁻¹ respectively. These peak shifts provided strong evidence of a chemical interaction between SA and Cu²⁺ ions.^[20]

The less swelling of SA and Cu-SA films in ethylene carbonate/propylene carbonate (EC/PC) organic solvent, which is important for effectively suppressing Cu-ion transport and fast Li-ion transport, was evaluated by measuring the weight increase after immersing of the SA, and Cu-SA films into the EC/PC solvent for 24 h. For comparison, the weight gain of poly(vinylidene fluoride) (PVDF) films in the same solvent was also evaluated. As shown in Figure 1d, weight increase of SA and Cu-SA film are 14.5% and 8.5%, respectively, while PVDF film with similar thickness absorbed a substantial amount of carbonate solvents and the weight increase reach to 42.4%. The low swellability of SA and Cu-SA ensures the high stability of Cu-SA layer on CuF₂ surface.

Since anhydrous CuF₂ is inevitably changed into the hydroxylated phase of CuF₂ when water is used as a solvent for electrode fabrication, the hydroxylated CuF₂ (H-CuF₂) was directly used as active materials. The electrochemical performance of hydroxylated CuF₂ electrodes that were prepared using water-SA slurry were evaluated and compared to anhydrous

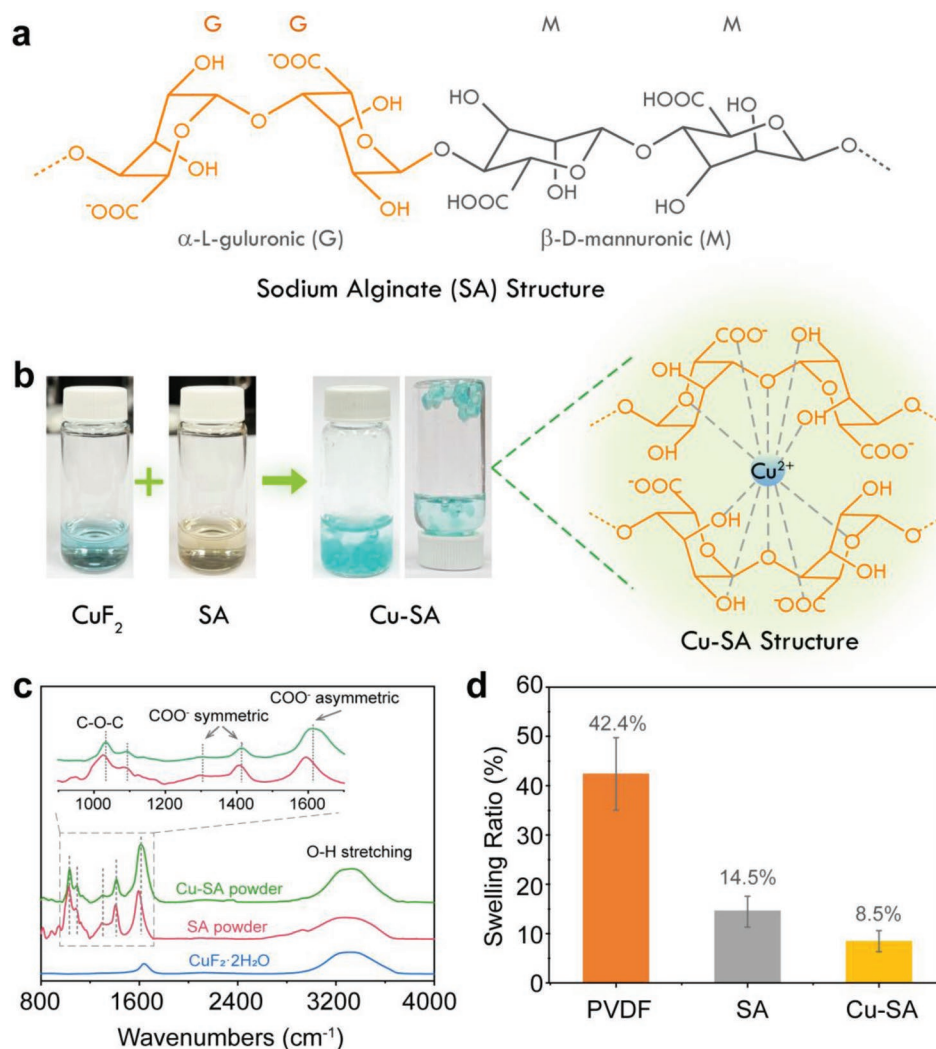


Figure 1. a) Chemical structure of sodium alginate (SA) chain. b) Digital images of the Cu-SA gel and the chemical structure of Cu-SA, visually demonstrating the cross-linking effect of SA and Cu^{2+} ions. c) Raman spectra of the dried SA and Cu-SA powder. d) Swelling ratios of PVDF, SA, and Cu-SA film in EC/PC solvent.

CuF_2 electrodes that were prepared using *N*-methylpyrrolidone (NMP)-PVDF slurry. Both anhydrous and hydroxylated CuF_2 were coated by carbon through ball-milling of CuF_2 -Ketjenblack (KB) mixture to enhance the reaction kinetics. Both commercial anhydrous (Figure S1a,b, Supporting Information) and hydrous (Figure S1e,f, Supporting Information) CuF_2 particles show irregular shape. The high-resolution transmission electron microscopy (HRTEM) image (Figure S1c,g, Supporting Information) demonstrated that the anhydrous and hydroxylated CuF_2 particles are polycrystalline. Their polycrystallinity can be further proved by the diffraction rings in corresponding SAED images (Figure S1d,h, Supporting Information). After high-energy ball-milled (HBM) with KB, the irregular particles were converted into agglomerates consisting of small CuF_2 nanocrystallites with an average size of ≈ 10 nm. More importantly, the small CuF_2 nanoparticles were linked and closely surrounded by KB nanoparticles, which forms a consecutive conductive network, and consequently has a great improvement on the electronic conductivity of CuF_2 . The

morphologies of carbon-coated anhydrous (Figure S2a,b, Supporting Information) and hydroxylated CuF_2 (Figure S2e,f, Supporting Information) nanoparticles were also characterized by TEM. Different from the primary samples, only one type of lattice fringe can be observed in a single particle while the corresponding SAED images are still shown in the form of multiple diffraction rings (Figure S2c,d,g,h, Supporting Information), indicating the single crystallinity of HBM CuF_2 nanoparticles. The phase structures of CuF_2 nanoparticles after HBM treatment were determined by X-ray powder diffraction (XRD). No additional peak can be observed for anhydrous CuF_2 samples after HBM treatment and all the peaks match well with monoclinic CuF_2 (JCPDS #42-1244), indicating the pure phase of anhydrous CuF_2 (Figure S3a, Supporting Information). However, new diffraction peaks related to layered $\text{Cu}(\text{OH})\text{F}$ (JCPDS #07-0306) were observed in HBM hydrous CuF_2 nanoparticles, which is due to the decomposition of partial hydrous CuF_2 at increased temperature during HBM process (Figure S3b, Supporting Information). Besides, the obviously broadened peak

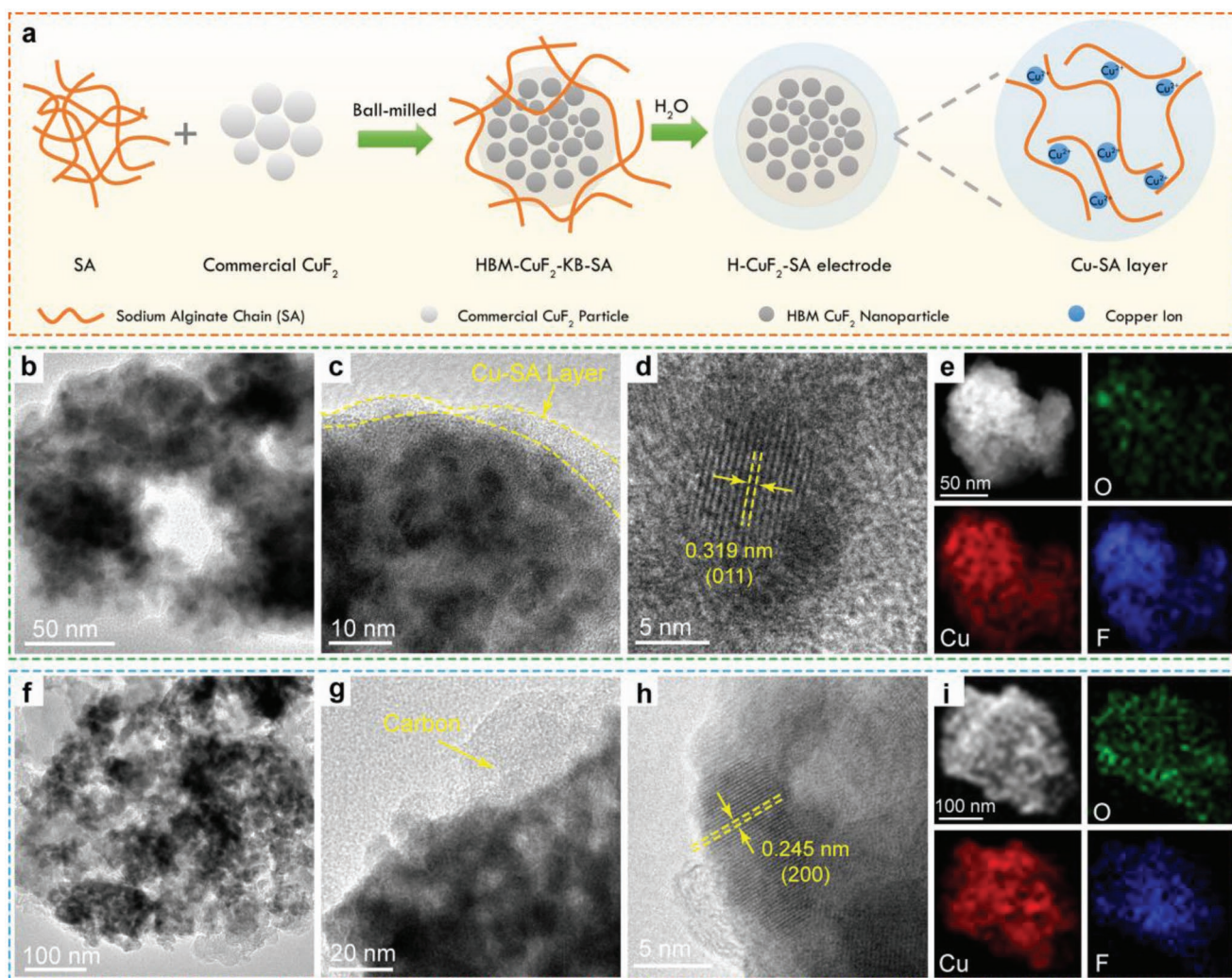


Figure 2. a) Schematic illustrations of the fabrication of H-CuF₂-SA electrodes. b,c) TEM images and d) HRTEM image of the pristine H-CuF₂-SA electrode nanoparticles. e) HAADF-STEM image of H-CuF₂-SA nanoparticles and the corresponding EDS mappings of Cu, F, and O elements. f,g) TEM images and h) HRTEM image of pristine H-CuF₂-PVDF electrode nanoparticles. i) HAADF-STEM image of H-CuF₂-PVDF electrode nanoparticles and the corresponding EDS mapping of Cu, F, and O elements.

breadth after HBM treatments also confirmed the nanocrystalline nature of these HBM CuF₂ samples.

Figure 2a illustrates the fabrication process of the hydroxylated CuF₂ electrodes with SA binder (denoted as H-CuF₂-SA electrode). Unlike the traditional electrode fabrication process, we didn't directly mix the SA aqueous solution with CuF₂ particles to avoid the rapid cross-linking effect between SA and Cu²⁺ ions. Instead, we ball-milled the SA powder with CuF₂ nanoparticles first to ensure the uniform dispersal of SA and close contact to CuF₂ particles. Then KB was added into the ball-milled CuF₂-SA mixture with further ball-milling to obtain the CuF₂-KB-SA nanoparticles (HBM-CuF₂-KB-SA) (Figure S4, Supporting Information). DI water, as the binder solvent, was dropwise added into the HBM-CuF₂-KB-SA mixture during continuous manual grinding. The low solubility of CuF₂ and slow dissolution process of SA can effectively prevent the rapid growth of large Cu-cross-linked SA hydrogels (Cu-SA), ensuring the in situ formation of a thin Cu-SA

layer on the surface of CuF₂-KB. TEM image of the H-CuF₂-SA electrode powder shows that the thickness of Cu-SA layer on the surface of CuF₂ is ≈5 nm (Figure 2b,c). The Cu-SA layer has amorphous structure as evidenced by HRTEM images (Figure 2c,d). The nanocrystalline in Figure 2d with a lattice plane spacing of 0.319 nm can be indexed to (011) lattice plane of Cu(OH)F. The phase change from anhydrous CuF₂·2H₂O to Cu(OH)F is attributed to the thermal decomposition of hydrous CuF₂·2H₂O during electrode drying process, which is consistent with corresponding XRD pattern (Figure S5, Supporting Information). The uniform distribution of Cu-SA and SA were also demonstrated by Cu, F, and O elemental mapping images (Figure 2e). For comparison, CuF₂·2H₂O-KB electrode without Cu-SA coating was also prepared by using PVDF binder and NMP solvent (denoted as H-CuF₂-PVDF electrode). Since PVDF binder in H-CuF₂-PVDF is hard to be observed, its morphology is almost the same as HBM-H-CuF₂-KB nanoparticles (Figure 2f,g and Figure S2e,f, Supporting Information).

The parallel lattice fringe in a single particle with a plane spacing of 0.245 nm, can be related to the (200) lattice plane of Cu(OH)F (Figure 2h). Meanwhile, the characteristic circular lattice fringes at the bottle of HRTEM image are the characteristic fringe of carbon black.

2.2. Electrochemical Performance of Cu-SA-Coated CuF₂ Cathodes

Figure 3a shows the cycle performance of H-CuF₂-SA, H-CuF₂-PVDF, and CuF₂-PVDF electrodes at 0.05 C. The capacity of CuF₂-PVDF faded rapidly to 104.5 mAh g⁻¹ after only five cycles, which is less than 20% of its initial capacity. The H-CuF₂-PVDF shows a better cycling stability than CuF₂-PVDF, but the capacity still dropped to 148.6 mAh g⁻¹ at 50 cycles. In sharp contrast, H-CuF₂-SA maintains a reversible capacity of 420.4 mAh g⁻¹ at 50 cycles at 0.05 C, which was never reported before. The long cycle stabilities of three electrodes at different C-rates were also evaluated (Figure 3b and Figure S6, Supporting Information). Both CuF₂-PVDF (Figure S6a, Supporting Information) and H-CuF₂-PVDF (Figure S6b, Supporting Information) deliver a poor cycling stability at all C-rates. However, H-CuF₂-SA (Figure 3f) can reach a capacity of 420.4 mAh g⁻¹ at 0.05 C and maintain 200.1 mAh g⁻¹ at a high rate of 1 C after 50 cycles, which is five to ten times higher than that of CuF₂-PVDF or H-CuF₂-PVDF.

The electrochemical performances of the H-CuF₂-SA, H-CuF₂-PVDF, and CuF₂-PVDF electrodes were investigated using galvanostatic charge/discharge at 0.05 C. Figure S7a, Supporting Information, shows the first three charge/discharge profiles of CuF₂-PVDF. The flat plateau at around 2.9 V in the first discharge is attributed to one-step reduction of CuF₂ forming metallic copper and lithium fluoride.^[21] The first discharge capacity of CuF₂-PVDF at 0.05 C is 540.2 mAh g⁻¹, which is higher than its theoretical capacity (528 mAh g⁻¹) due to the parasitic reactions between electrolyte and electrode.^[22] In the first charge process, two slope plateaus at around 3.4 and 3.7 V are observed, which can be related to the oxidation of Cu(0) to form Cu(I) intermediates at 3.4 V, and the oxidation of both Cu(0) and Cu(I) to Cu(II) products at 3.7 V.^[7b] The high oxidation plateau at 3.7 V is mainly attributed to the reconversion to CuF₂. However, electrochemical oxidation of Cu into Cu ions and dissolution of Cu ions into electrolyte also contribute to the capacity due to similar thermodynamic potential of ≈3.5 V.^[23] The low first charge capacity of 407.8 mAh g⁻¹ is mainly caused by the incomplete reaction of Cu particles with LiF matrix and Cu-ion dissolution. Since the dissolution of active materials in charge process is irreversible, the second discharge capacity of CuF₂ cathode drop to 272.5 mAh g⁻¹. The increased discharge plateau of CuF₂-PVDF at 3.1 V in the second discharge is attributed to the increase of reaction kinetics due to the decreased particle size. The discharge capacities of CuF₂-PVDF faded quickly to 31.8% of capacity after the first three cycles due to the serious copper dissolution.

Different from that of CuF₂-PVDF, the first galvanostatic discharge profiles of H-CuF₂-SA and H-CuF₂-PVDF show a long plateau around 2.0 V, reaching a high specific capacity of 622.8 and 588.3 mAh g⁻¹ at 0.05 C, respectively (Figure 3c

and Figure S7b, Supporting Information). The lower reduction potential is due to the lower electronegativity of Cu–OH than Cu–F, which reduces the activation energy barrier for the conversion of copper fluorides.^[3a,18,24] In the following charge profiles, both H-CuF₂-PVDF and H-CuF₂-SA show a small plateau at 3.2 V and a large slope plateau around 3.7 V. Similar to the anodic reaction of CuF₂-PVDF, the small plateau at 3.2 V is attributed to the oxidation of Cu metal to Cu(I) intermediates, and the larger slope plateau at 3.7 V is ascribed to the formation of Cu(OH)F. In the second and following discharge, both H-CuF₂-SA and H-CuF₂-PVDF electrodes show a high discharge potential around 3.1 and 2.1 V. The discharge capacities of H-CuF₂-PVDF decayed quickly due to the dissolution of Cu ions in the electrolyte during the charging process. It is worth mentioning that the capacity at 3.1 V decayed faster in the initial cycles due to the larger energy barrier of LiF formation. Since the Cu-SA coating layer suppressed Cu-cation dissolution, H-CuF₂-SA shows a stable capacity (Figure 3c). The reversible conversion of H-CuF₂-SA was further demonstrated by the charge–discharge profiles with normalized capacity (Figure 3d). After 50 cycles, the reduction potentials of H-CuF₂-SA at around 3.0 and 2.1 V can still be clearly observed, whereas the reduction reaction at 3.0 V almost disappeared after 20 cycles for H-CuF₂-PVDF and CuF₂-PVDF cells (Figure S8, Supporting Information).

The electrochemical behaviors of CuF₂-PVDF, H-CuF₂-SA, and H-CuF₂-PVDF electrodes were also evaluated using cyclic voltammetry (CV) at a scan rate of 0.1 mV s⁻¹ in the voltage range of 1.5–4.4 V. As shown in Figure S9, Supporting Information, all three fluoride electrodes exhibit a lithiation reaction peak of Cu–F at around 3.0 V, while H-CuF₂-PVDF and H-CuF₂-SA show an additional sharp peak at lower potential of 2.0 V, corresponding to the lithiation of the hydroxylated part of CuF₂. Different from anhydrous CuF₂, hydrated fluorides exhibit two additional small peaks below 3.0 V during delithiation. Both H-CuF₂-PVDF and H-CuF₂-SA also have a low oxidation peak (3.4 V) than that (3.7 V) of CuF₂-PVDF. These results indicate that LiOH has a lower reaction activation energy barrier than that of LiF, which is consistent with their galvanostatic profiles. The CV profiles of three electrodes are consistent with the galvanostatic charge/discharge behavior (Figure 3c and Figure S7, Supporting Information) of three electrodes.

Besides, H-CuF₂-SA also shows much higher rate capability than those of H-CuF₂-PVDF and CuF₂-PVDF (Figure 3e). At a low rate of 0.05 C, all three electrodes deliver similar first discharge capacity of ≈600 mAh g⁻¹. When the current density increased to 0.1, 0.2, 0.5, and 1 C, H-CuF₂-SA retains a reversible capacity of 409.4, 335.8, 257.8, and 203.3 mAh g⁻¹, respectively. When the current density returned to 0.05 C, the cell showed a stable and reversible discharge capacity of 392.5 mAh g⁻¹, demonstrating excellent cycling stability and rate tolerance. However, H-CuF₂-PVDF delivers only 341.5, 271.8, 129.7, 79.7, and 58.1 mAh g⁻¹ at the same rates, and capacity of CuF₂-PVDF quickly decay to <100 mAh g⁻¹ in five cycles at a low rate of 0.05 C before changing the C rate.

Figure 3f compared CuF₂-based conversion cathodes reported to date. All reported CuF₂-based conversion cathodes rapidly dropped in the first ten cycles at a high rate of 0.2 C or at extremely low current density of 0.02 C.^[7a,9,11,12,18] In sharp

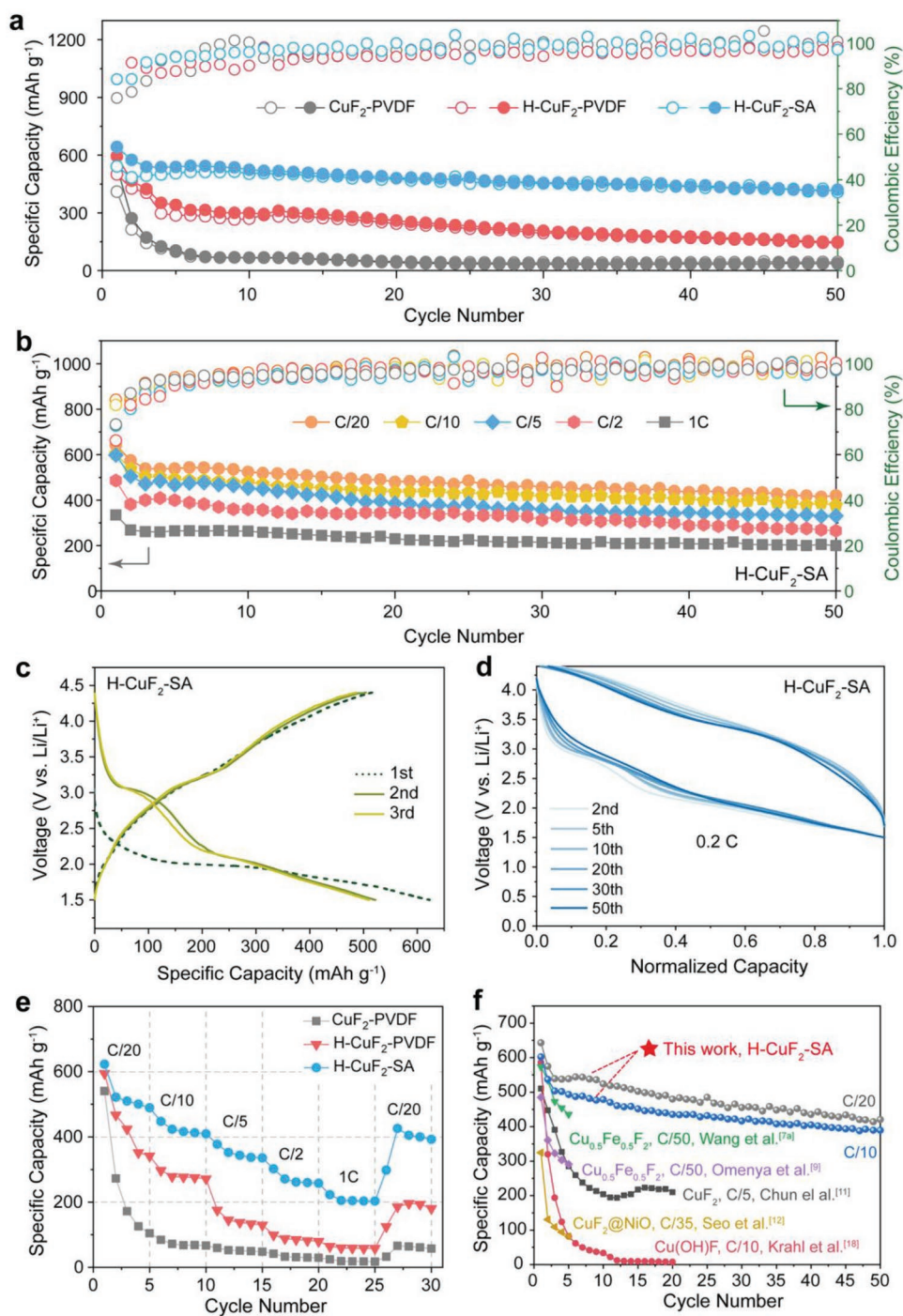


Figure 3. Electrochemical performance of anhydrous CuF_2 and hydroxylated CuF_2 cathodes using different binders. a) Long-cycle performance of CuF_2 -PVDF, H- CuF_2 -PVDF, and H- CuF_2 -SA cathodes at 0.05 C. b) Cycle stabilities of H- CuF_2 -SA at different C rates. c) Charge-discharge profiles of H- CuF_2 -SA at 0.05 C ($1\text{ C} = 539\text{ mAh g}^{-1}$). d) The normalized charge-discharge profiles of H- CuF_2 -SA electrode at 0.2 C. e) Rate performance of CuF_2 -PVDF, H- CuF_2 -PVDF, and H- CuF_2 -SA cathodes. f) Cycle performance comparison with previous studies of other CuF_2 or Cu-based fluorides cathodes.

contrast, H- CuF_2 -SA can achieve 50 reversible cycles and maintain a capacity of 420.4 mAh g^{-1} , demonstrating a superior cyclic stabilities among all CuF_2 -based cathodes. The in situ cross-linked Cu-SA layer on H- CuF_2 during electrode fabricating process is simple and very effective in enhancing the cycling stability.

In order to get a further understanding on the mechanism for reaction kinetic decay of H- CuF_2 -SA electrodes, electrochemical impedance spectroscopy (EIS) tests were conducted on all electrodes before and after cycling (Figure S10, Supporting Information). EIS of three electrodes consist of depressed semicircles in the high-frequency region and a slope

in the low-frequency region, which can be ascribed to interface resistance (R_{int}) and ion diffusion resistance (R_w) respectively. The fresh three electrodes have similar interface resistances (R_{int}). After 50 charge/discharge cycles, the interface resistances of all three electrodes increase. At 50th cycle, the H-CuF₂-PVDF has the largest interface resistance followed with CuF₂-PVDF, while H-CuF₂-SA has the lowest interface resistance. The R_{int} value of fresh electrodes and cycled electrodes were calculated (Table S1, Supporting Information) using the equivalent circuit. The interface resistance of CuF₂-PVDF and H-CuF₂-PVDF increase significantly, which is caused by active materials loss and the continuous copper coprecipitation on Li anode.^[25]

2.3. The Reversibility of Conversion Reaction of Cu-SA-Coated CuF₂ Cathodes

The phase change and reaction reversibility of H-CuF₂-SA were investigated by XRD (Figure 4a). When the H-CuF₂-SA was fully discharged to 1.5 V, peak located at 18.7° related to (001) plane of Cu(OH)F disappeared, while an obvious broad peak corresponding to (111) plane of Cu around 43.2° arose, suggesting the full conversion of Cu(OH)F. It is worth noting that no other peaks of LiF or LiOH can be observed at the first

discharged state due to their low crystallinity and overlapped peak positions with Cu and Ti. The peaks of Cu(OH)F were recovered when the cell was fully charged, indicating the reversible reactions of Cu(OH)F. However, a small but sharp peak of Cu still can be found, suggesting that a trace amount of inactive Cu particles remained in electrode. After 50 cycles, the diffraction peak of Cu is a combination of a large broad peak and a small sharp peak, indicating that Cu particles size did not grow into severe coarsen after long cycles, which ensures the good cycling performance of H-CuF₂-SA electrode.

The existence of LiF and LiOH were further proved by the HRTEM image and corresponding fast Fourier transformed (FFT) patterns (Figure 4b–d). Due to the superimposed distribution of Cu, LiF, and LiOH nanoparticles, their lattice planes in the HRTEM image are overlapped and hard to be distinguished (Figure 4b). Herein, FFT analyses were conducted in two selected regions (red boxes in Figure 4b) of HRTEM image to clarify the existence of LiF and LiOH. The corresponding FFT pattern of region I show three sets of diffraction spots, indicating a polycrystalline distribution of this region (Figure 4c). The brightest diffraction spots with a lattice plane distance of 0.208 nm are related to the (111) plane of highly crystalline Cu, which is consistent with the XRD results. The darker spot besides them with a slightly lower lattice distance

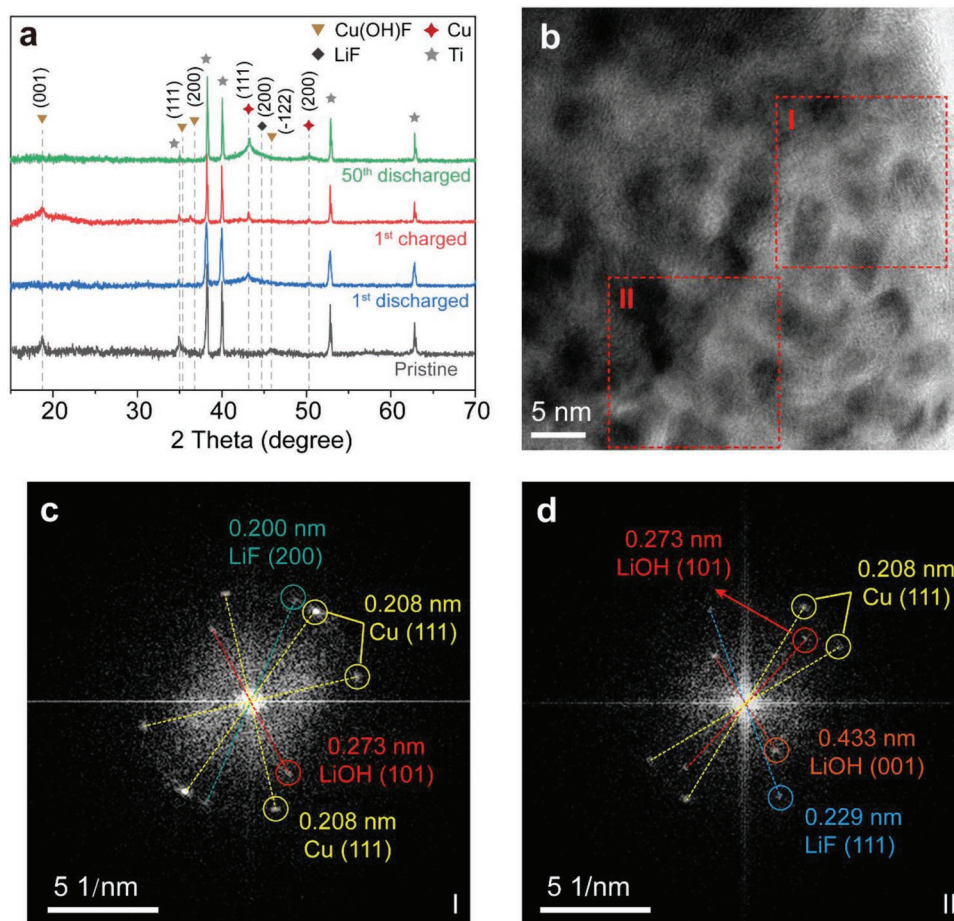


Figure 4. a) XRD patterns of H-CuF₂-SA cathode at different charge/discharge state. b) HRTEM image of H-CuF₂-SA cathode after first discharge. c,d) Corresponding FFT patterns of region I (c) and region II (d).

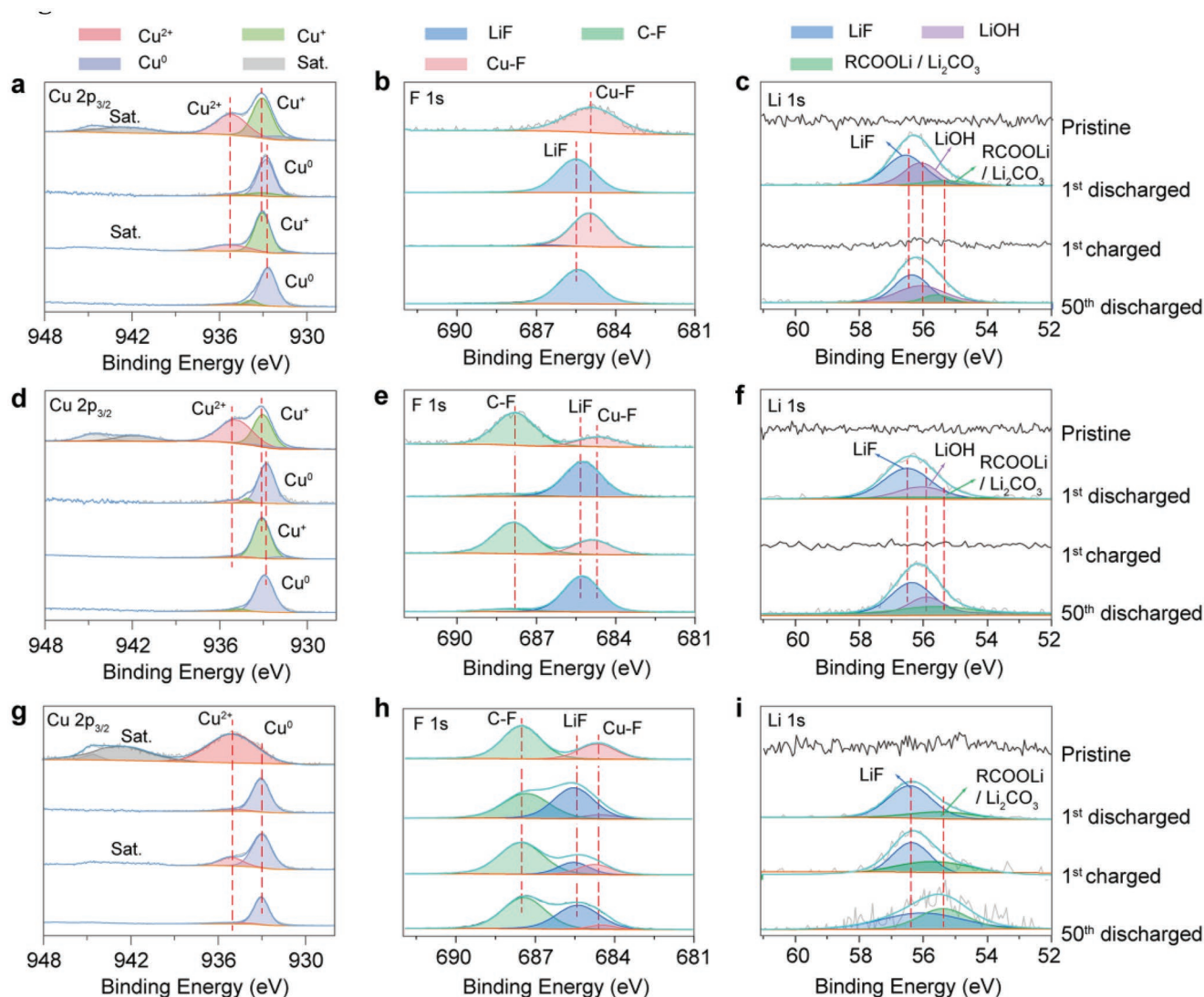


Figure 5. a–i) XPS spectra of Cu 2p_{3/2}, F 1s, and Li 1s of H-CuF₂-SA (a–c), H-CuF₂-PVDF (d–f), and CuF₂-PVDF (g–i) electrodes before and after cycling, respectively. Each spectrum was tested from the surface of electrodes.

can be indexed to the (200) plane of LiF. Since the (111) plane has the largest plane distance of Cu, diffraction spots showing larger plane distance can be easily distinguished with Cu. Therefore, in both region I and II, the diffraction spots located in a smaller circle can be indexed to the (111) plane of LiF and (101) and (001) plane of LiOH, respectively, according to their characteristic lattice distance (Figure 4c,d).

XPS analysis was performed on pristine and cycled CuF₂-PVDF, H-CuF₂-PVDF, and H-CuF₂-SA electrodes to reveal their reversibility (Figure 5). For two hydrous pristine H-CuF₂-SA (Figure 5a) and H-CuF₂-PVDF (Figure 5d) electrodes, the Cu 2p_{3/2} spectra can be well simulated into two peaks located at 933.1 and 935.2 eV, which can be ascribed to the Cu⁺ and Cu²⁺ oxidation state, respectively, indicating the multivalence properties of copper in Cu(OH)F.^[26] Whereas only one single peak located at 935.7 eV related to Cu²⁺-F was observed in pristine CuF₂-PVDF electrodes (Figure 5g). When the cell was first discharged to 1.5 V, the Cu 2p_{3/2} spectra were shifted to 932.6 eV

for all three electrodes, which can be indexed to metallic Cu⁰, demonstrating the fully reduction of these fluoride electrodes.^[27] At the first fully charged state, Cu²⁺ and Cu⁺ valence states in the pristine sample were recovered in H-CuF₂-SA electrode, demonstrating its good reversibility of conversion reaction. However, Cu²⁺ signal almost disappeared in H-CuF₂-PVDF due to the serious copper dissolution in charge process at the electrode surfaces, which is in line with its charge-discharge performance. As for anhydrous CuF₂-PVDF electrode, the existence of Cu⁰ peaks reveals that only part of metallic copper was reconverted to CuF₂ due to the coarsening of Cu particles. Similar results were also observed in the F 1s spectra. The Cu-F signal in pristine electrode was completely converted to Li-F at discharge state and recovered at fully charged state in H-CuF₂-PVDF and H-CuF₂-SA electrode, while both Li-F and Cu-F signals can be detected in CuF₂-PVDF electrode at different lithiation states. The incomplete conversion of pure CuF₂ is mainly caused by the interruption of electronic

transportation between conductive metallic Cu and isolative LiF aggregates, which lead to a lot of “dead” active materials in the CuF_2 -PVDF electrode. Li 1s spectra at the discharged state reveals the different conversion reaction path between pure CuF_2 and hydroxylated CuF_2 (Figure 5c,f,i). Both Li–F and Li–OH can be detected in Li 1s spectra of H- CuF_2 -PVDF and H- CuF_2 -SA electrode at discharged state, providing strong evidence that a mixture of LiF and LiOH was formed in the reduction reaction rather than pure LiF. The existence of LiOH effectively lowers the free enthalpy of the conversion reaction, thus ensuring a more thorough reaction of $\text{Cu}(\text{OH})\text{F}$ than pure CuF_2 cathode materials.

2.4. Cu-Ion Dissolution Suppression by Cu-SA Coating

The Cu particle growth and stability of Cu-SA coating layer after 50 cycles were also characterized by TEM. As shown in Figure S11, Supporting Information, the reduction products of metallic Cu in H- CuF_2 -PVDF electrodes after 50 cycles showed an uneven size range from 5 to 50 nm. In contrast, Cu particles in H- CuF_2 -SA still maintained a uniform distribution with an average size of ≈ 5 nm, which is line with the XRD results above. In addition, the Cu-SA layer is still clearly visible after 50 cycles, serving as a preformed CEI layer which can assist in improving the structure stability of H- CuF_2 -SA electrode during long-time cycling.

Since the dissolution of Cu ions in the electrolyte will be deposited on Li anode, it can be analyzed using SEM and

EDS. As shown in Figure 6a,b, the cycled Li anode coupled with H- CuF_2 -SA cathode showed smooth surface with only a few salt residues visible, which were further proved by the C and O elemental mapping images displayed in Figure 6c. In the meantime, the Cu elemental mapping image displayed in Figure 6c shows random distributed dots with pale pink color, which can be ascribed to the background noise. No trace of Cu signal could be observed in the corresponding EDS spectra (Figure 6g), suggesting that no significant copper dissolution happens during the lithiation/delithiation of H- CuF_2 -SA cathodes. In a sharp contrast, SEM image of Li anode after cycling with H- CuF_2 -PVDF cathodes showed extremely rough surface, and sumless Cu particles were plated on the Li surface (Figure 6d,e). Bright pink spots in the Cu elemental mapping image and strong Cu peaks in corresponding EDS spectra further revealed significant content of Cu (Figure 6f,h), indicating the serious copper dissolution in H- CuF_2 -PVDF cathode. Furthermore, since the rough surface of Li anode is correlated with Cu metal coprecipitation, it could be suggested that the reduction of Cu ions destroyed the uniformity of SEI on Li anode and led to the surface roughening. Transition metal dissolution and disposition in the SEI on graphite during charge/discharge cycles of lithiated transition metal cathode/graphite cell were also reported. Here, the copper dissolution is more serious in CuF_2 electrodes.^[25c]

The comprehensive characterizations and electrochemical analysis of H- CuF_2 -SA cathode demonstrated that the super cycling stability of H- CuF_2 -SA cathode is attributed to unique Cu-SA coating layer that is in situ formed in electrode

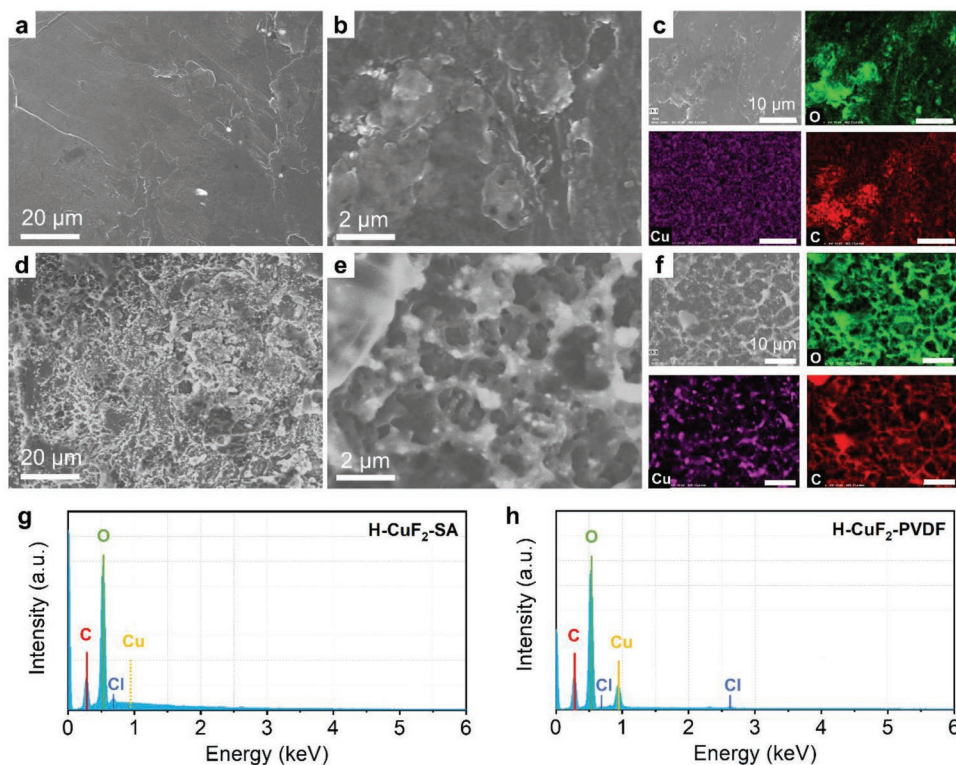


Figure 6. a–f) SEM images and corresponding Cu, O, and C elemental mapping images of Li anode after 50 cycles with H- CuF_2 -SA cathode (a–c) and H- CuF_2 -PVDF cathode (d–f). g,h) EDS spectra of Li anode surface after cycling with H- CuF_2 -SA (g) and H- CuF_2 -PVDF (h) cathode.

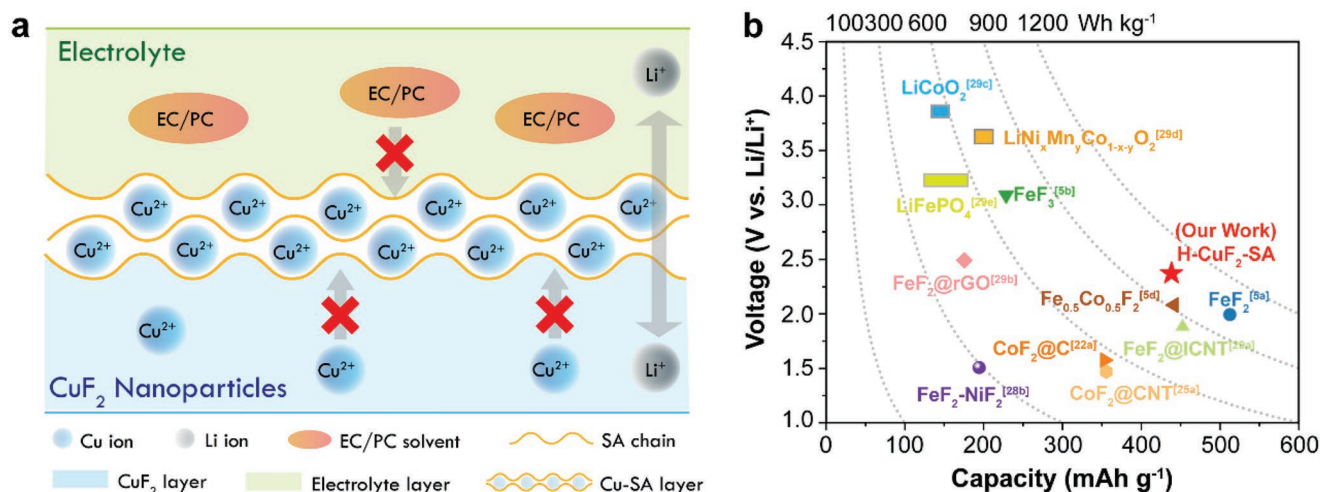


Figure 7. a) Schematic illustration of the working mechanism of the SA binder for enhanced electrochemical performance of the H-CuF₂-SA cathode. b) Capacity, voltage, and energy density of H-CuF₂-SA (discharge energy density is calculated based on a discharge current of 0.05 C) as compared with other metal fluorides and intercalation cathodes.

fabrication process. **Figure 7a** schematically illustrates the formation and function of Cu-SA coating layer on H-CuF₂ particles. In the electrode fabrication process, a robust Cu-SA layer was in situ formed on the surface of CuF₂ particles due to the strong cross-link effect between SA chain and copper ions in aqueous solution. The Cu-SA layer is selectively permeable to Li⁺ but is impermeable to Cu²⁺, which effectively suppress the Cu-ion dissolution and degradation. Besides, the low swellability of both Cu-SA layer and SA binder in the carbonate electrolyte solvent reduced the electrode/electrolyte interaction, preventing undesirable access of the electrolyte liquid to the binder/electrode interface, thus further reducing the possibility of copper dissolution in the electrode. In addition, the Cu-SA coating cross-linked into matrix with high rigidity, which maintain the structure stability of H-CuF₂-SA electrode during the lithiation/delithiation process, ensuring excellent stability of H-CuF₂-SA electrode with superior reversible capacity. Although the aqueous-based SA binder introduced hydrated impurities into CuF₂ cathode material, H-CuF₂-SA cathode can still provide an average discharge potential above 2.4 V. The high capacity combined with a high discharge voltage leads to a reversible discharge energy density of ≈1009.1 Wh kg⁻¹ at current density of 0.05 C after 50 cycles (**Figure 7b**), which is higher than most of conversion metal fluorides, such as FeF₃, FeF₂, NiF₂, and CoF₂ (Table S2, Supporting Information).^[25a,28] More importantly, the energy density of H-CuF₂-SA in this work is higher than most iron-based fluorides and commercial intercalation cathode materials.^[5a,b,d,7a,22a,28b,29] The significant improvement of cycling stability from 5 to 50 cycles for copper-based fluoride cathode demonstrated the breakthrough from irreversible to reversible.

3. Conclusion

We successfully suppress the Cu-ion dissolution in CuF₂ cathode by in situ formation of a Cu²⁺-coordinated SA layer on the surface of CuF₂ nanoparticles during the electrode

fabricating process. The Cu-SA cross-linked layer can selectively enable the transportation of Li ions while blocking the mobility of Cu ions, as well as reducing the undesirable interaction between electrolyte/electrode interface due to its low swellability and high rigidity in carbonate electrolyte. The obtained H-CuF₂-SA electrode delivered a reversible capacity of 420.4 mAh g⁻¹ at 0.05 C after 50 cycles and reached a high energy density of 1009.1 Wh kg⁻¹. The superior cycling stability and energy densities demonstrate the best performance of Cu-based fluoride cathode. The Cu-ion cross-linking strategy opens the door for CuF₂ to serve as a high energy, low cost, and reversible cathode for next-generation Li-ion batteries.

4. Experimental Section

Synthesis of Carbon-Coated CuF₂ Nanoparticles (CuF₂-KB): The CuF₂-KB nanoparticles were prepared by HBM method. 1.8 g of a mixture composed of CuF₂ and KB (60:30 wt%) was ball-milled under an argon atmosphere in SPEX 8000 by using zirconia ceramic grinding vial and balls for 4 h.

Synthesis of Carbon-Coated Hydrated CuF₂ Nanoparticles (H-CuF₂-KB): The H-CuF₂-KB nanoparticles were prepared by ball-milled a mixture of CuF₂·2H₂O and KB (81:30 wt%) with the same HBM procedure.

Synthesis of Sodium Alginate Pre-Mixed Carbon-Coated CuF₂ Nanocomposites (CuF₂-KB-SA): The CuF₂-KB-SA nanocomposites were also prepared by HBM. First, 1.5 g of a mixture composed of CuF₂ and SA (60:10 wt%) was ball milled for 1 h, then 0.6 g KB was added into the ball-milling jar under an argon atmosphere, and the whole mixture was ball-milled for another 3 h.

Materials Characterization: The powder XRD data were collected with a Bruker D8 X-ray diffractometer using Cu K α radiation ($\lambda = 1.5418 \text{ \AA}$). SEM and HRTEM images were taken using Hitachi SU-70 analytical GEG SEM (Japan) and JOEL JEM (Japan) 2100 LaB6 transmission electron microscope with an electron accelerating voltage of 200 KeV, respectively. FTIR was recorded by NEXUS 670 FTIR instrument. XPS data were collected using a high-sensitivity X-ray photoelectron spectrometer (Kratos AXIS 165, Mg K α radiation). Raman measurements were performed on a Horiba Jobin Yvon Labram Aramis using a 532 nm diode-pumped solid-state laser.

Electrochemical Measurement: The CuF₂-PVDF electrode was prepared by mixing a 90:10 weight ratio of CuF₂-KB and PVDF in NMP. The

H-CuF₂-PVDF electrode was prepared by mixing a 121:10 weight ratio of H-CuF₂-KB and PVDF. To prepare the H-CuF₂-SA electrode, 200 mg of CuF₂-SA-KB powder was added into the agate mortar, and then the DI water was added drop wisely into the mortar with manual grinding to obtain the uniform slurry. All the slurries were casted on titanium foil and dried at 80 °C overnight. The average active mass loading of electrodes was ≈0.8–1.0 mg cm⁻². The electrodes were applied as cathode with lithium foils as anodes and glass fiber (GF/A) as the separator, and the electrolyte was 4 m lithium perchlorate (LiClO₄) in EC/PC 50:50 by the volume. The coin cells (CR2032) were assembled in an Argon-filled glovebox (<0.1 ppm of H₂O, <0.1 ppm of O₂). Electrochemical performance was tested with a NEWARE testing system. The cells were charged and discharged between a voltage range of 1.5–4.4 V. The CV and EIS were conducted on a CHI 660E electrochemical workstation (CHI Instruments Inc. USA) with a scan rate of 0.1 mV s⁻¹ between 1.5 and 4.4 V.

Supporting Information

Supporting Information is available from the Wiley Online Library or from the author.

Acknowledgements

J.X. and Z.W. contributed equally to this work. The authors thank Dr. Sz-Chian Liou from the Advanced Imaging and Microscopy Laboratory at the University of Maryland for help in microscope operation. J.X. acknowledges the China Scholarship Council for financial support.

Conflict of Interest

The authors declare no conflict of interest.

Data Availability Statement

The data that support the findings of this study are available in the supplementary material of this article.

Keywords

copper fluoride, cross-link effect, hydroxylated copper fluoride, Li-ion batteries, sodium alginate

Received: June 9, 2022

Revised: August 8, 2022

Published online:

- [1] J. M. Tarascon, M. Armand, *Nature* **2001**, 414, 359.
 [2] a) M. S. Whittingham, *Chem. Rev.* **2014**, 114, 11414; b) V. Etacheri, R. Marom, R. Elazari, G. Salitra, D. Aurbach, *Energy Environ. Sci.* **2011**, 4, 3243.
 [3] a) F. Wu, G. Yushin, *Energy Environ. Sci.* **2017**, 10, 435; b) Y. Jiang, J. L. Yue, Q. Guo, Q. Xia, C. Zhou, T. Feng, J. Xu, H. Xia, *Small* **2018**, 14, 1704296.
 [4] L. Wang, Z. Wu, J. Zou, P. Gao, X. Niu, H. Li, L. Chen, *Joule* **2019**, 3, 2086.
 [5] a) A. W. Xiao, H. J. Lee, I. Capone, A. Robertson, T. U. Wi, J. Fawdon, S. Wheeler, H. W. Lee, N. Grobert, M. Pasta, *Nat. Mater.* **2020**, 19,

- 644; b) F. Wu, V. Srot, S. Chen, S. Lorger, P. A. van Aken, J. Maier, Y. Yu, *Adv. Mater.* **2019**, 31, 1905146; c) Q. Huang, K. Turcheniuk, X. Ren, A. Magasinski, D. Gordon, N. Bensalah, G. Yushin, *Adv. Energy Mater.* **2019**, 9, 1803323; d) X. Fan, E. Hu, X. Ji, Y. Zhu, F. Han, S. Hwang, J. Liu, S. Bak, Z. Ma, T. Gao, S. C. Liou, J. Bai, X. Q. Yang, Y. Mo, K. Xu, D. Su, C. Wang, *Nat. Commun.* **2018**, 9, 2324; e) T. Chen, H. Kaur, M. McCrystall, R. Tian, A. Roy, R. Smith, D. V. Horvath, J. Maughan, B. Konkena, M. Venkatesan, K. Synnatschke, T. Carey, J. Liu, J. Pepper, R. Zhang, C. Baces, V. Nicolosi, H. Xia, J. N. Coleman, *FlatChem* **2022**, 33, 100360.
 [6] G. G. Amatucci, N. Pereira, *J. Fluorine Chem.* **2007**, 128, 243.
 [7] a) F. Wang, S. W. Kim, D. H. Seo, K. Kang, L. Wang, D. Su, J. J. Vajo, J. Wang, J. Graetz, *Nat. Commun.* **2015**, 6, 6668; b) X. Hua, R. Robert, L. S. Du, K. M. Wiaderek, M. Leskes, K. W. Chapman, P. J. Chupas, C. P. Grey, *J. Phys. Chem. C* **2014**, 118, 15169.
 [8] F. Wang, R. Robert, N. A. Chernova, N. Pereira, F. Omenya, F. Badway, X. Hua, M. Ruotolo, R. Zhang, L. Wu, V. Volkov, D. Su, B. Key, M. S. Whittingham, C. P. Grey, G. G. Amatucci, Y. Zhu, J. Graetz, *J. Am. Chem. Soc.* **2011**, 133, 18828.
 [9] F. Omenya, N. J. Zagarella, J. Rana, H. Zhang, C. Siu, H. Zhou, B. Wen, N. A. Chernova, L. F. J. Piper, G. Zhou, M. S. Whittingham, *ACS Appl. Energy Mater.* **2019**, 2, 5243.
 [10] a) F. Badway, A. Mansour, N. Pereira, J. Al-Sharab, F. Cosandey, I. Plitz, G. Amatucci, *Chem. Mater.* **2007**, 19, 4129; b) A. N. Mansour, F. Badway, W. S. Yoon, K. Y. Chung, G. G. Amatucci, *J. Solid State Chem.* **2010**, 183, 3029.
 [11] J. Chun, C. Jo, S. Sahgong, M. G. Kim, E. Lim, D. H. Kim, J. Hwang, E. Kang, K. A. Ryu, Y. S. Jung, Y. Kim, J. Lee, *ACS Appl. Mater. Interfaces* **2016**, 8, 35180.
 [12] J. K. Seo, H.-M. Cho, K. Takahara, K. W. Chapman, O. J. Borkiewicz, M. Sina, Y. S. Meng, *Nano Res.* **2017**, 10, 4232.
 [13] a) D. W. O'Connell, C. Birkinshaw, T. F. O'Dwyer, *Bioresour. Technol.* **2008**, 99, 6709; b) S. Thakur, B. Sharma, A. Verma, J. Chaudhary, S. Tamulevicius, V. K. Thakur, *J. Cleaner Prod.* **2018**, 198, 143.
 [14] Y. Chen, J. Feng, M. Fang, X. Wang, Y. Liu, S. Li, L. Wen, Y. Zhu, L. Jiang, *ACS Appl. Polym. Mater.* **2021**, 3, 3902.
 [15] a) I. Kovalenko, B. Zdyrko, A. Magasinski, B. Hertzberg, Z. Milicev, R. Burtovyy, I. Luzinov, G. Yushin, *Science* **2011**, 334, 75; b) J. Li, R. Lewis, J. Dahn, *Electrochim. Solid-State Lett.* **2006**, 10, A17; c) M. H. Ryou, J. Kim, I. Lee, S. Kim, Y. K. Jeong, S. Hong, J. H. Ryu, T. S. Kim, J. K. Park, H. Lee, J. W. Choi, *Adv. Mater.* **2013**, 25, 1571.
 [16] S.-J. Zhang, Y.-P. Deng, Q.-H. Wu, Y. Zhou, J.-T. Li, Z.-Y. Wu, Z.-W. Yin, Y.-Q. Lu, C.-H. Shen, L. Huang, S.-G. Sun, *ChemElectroChem* **2018**, 5, 1321.
 [17] a) Z.-Y. Wu, L. Deng, J.-T. Li, Q.-S. Huang, Y.-Q. Lu, J. Liu, T. Zhang, L. Huang, S.-G. Sun, *Electrochim. Acta* **2017**, 245, 371; b) H. Huang, R. Chen, S. Yang, W. Zhang, Y. Fang, L. Li, Y. Liu, J. Huang, *Synth. Met.* **2019**, 247, 212.
 [18] T. Krahl, F. M. Winkelmann, A. Martin, N. Pinna, E. Kemnitz, *Chem. - Eur. J.* **2018**, 24, 7177.
 [19] L. Iskandar, L. Rojo, L. Di Silvio, S. Deb, *J. Biomater. Appl.* **2019**, 34, 573.
 [20] a) S. K. Papageorgiou, E. P. Kouvelos, E. P. Favvas, A. A. Sapalidis, G. E. Romanos, F. K. Katsaros, *Carbohydr. Res.* **2010**, 345, 469; b) J. Liu, M. Sun, Q. Zhang, F. Dong, P. Kaghazchi, Y. Fang, S. Zhang, Z. Lin, *J. Mater. Chem. A* **2018**, 6, 7382.
 [21] N. Yamakawa, M. Jiang, C. P. Grey, *Chem. Mater.* **2009**, 21, 3162.
 [22] a) F. Wu, V. Srot, S. Chen, M. Zhang, P. A. van Aken, Y. Wang, J. Maier, Y. Yu, *ACS Nano* **2020**, 15, 1509; b) S. Kim, J. Liu, K. Sun, J. Wang, S. J. Dillon, P. V. Braun, *Adv. Funct. Mater.* **2017**, 27, 1702783.
 [23] a) Y. Huang, W. Zhang, S. Li, W. Luo, Z. Huang, C. Fang, M. Weng, J. Zheng, F. Pan, Q. Liu, Y. Huang, *Nano Energy* **2018**, 54, 59; b) H. Li, P. Balaya, J. Maier, *J. Electrochem. Soc.* **2004**, 151, A1878.
 [24] S.-K. Jung, H. Kim, M. G. Cho, S.-P. Cho, B. Lee, H. Kim, Y.-U. Park, J. Hong, K.-Y. Park, G. Yoon, W. M. Seong, Y. Cho, M. H. Oh,

- H. Kim, H. Gwon, I. Hwang, T. Hyeon, W.-S. Yoon, K. Kang, *Nat. Energy* **2017**, *2*, 16208.
- [25] a) X. Wang, W. Gu, J. T. Lee, N. Nitta, J. Benson, A. Magasinski, M. W. Schauer, G. Yushin, *Small* **2015**, *11*, 5164; b) Y. Dai, L. Cai, R. E. White, *J. Power Sources* **2014**, *247*, 365; c) C. Zhan, T. Wu, J. Lu, K. Amine, *Energy Environ. Sci.* **2018**, *11*, 243.
- [26] Y. Wang, Y. Lü, W. Zhan, Z. Xie, Q. Kuang, L. Zheng, *J. Mater. Chem. A* **2015**, *3*, 12796.
- [27] X. Wang, B. Zhang, W. Zhang, M. Yu, L. Cui, X. Cao, J. Liu, *Sci. Rep.* **2017**, *7*, 1584.
- [28] a) C. Villa, S. Kim, Y. Lu, V. P. Dravid, J. Wu, *ACS Appl. Mater. Interfaces* **2019**, *11*, 647; b) Q. Huang, T. P. Pollard, X. Ren, D. Kim, A. Magasinski, O. Borodin, G. Yushin, *Small* **2019**, *15*, e1804670.
- [29] a) Q. Huang, K. Turcheniuk, X. Ren, A. Magasinski, A. Y. Song, Y. Xiao, D. Kim, G. Yushin, *Nat. Mater.* **2019**, *18*, 1343; b) D. Ni, W. Sun, C. Lu, Z. Wang, J. Qiao, H. Cai, C. Liu, K. Sun, *J. Power Sources* **2019**, *413*, 449; c) Y. Lyu, X. Wu, K. Wang, Z. Feng, T. Cheng, Y. Liu, M. Wang, R. Chen, L. Xu, J. Zhou, Y. Lu, B. Guo, *Adv. Energy Mater.* **2020**, *11*, 2000982; d) J. Zheng, S. Myeong, W. Cho, P. Yan, J. Xiao, C. Wang, J. Cho, J. G. Zhang, *Adv. Energy Mater.* **2016**, *7*, 1601284; e) Z. Li, J. Yang, T. Guang, B. Fan, K. Zhu, X. Wang, *Small Methods* **2021**, *5*, 2100193.